Increase of Fe solubility in ZnO induced by the grain boundary adsorption

**S. G. Protasova · B. B. Straumal · A. A. Mazilkin ·
S. V. Stakhanova · P. B. Straumal ·
B. Baretzky**

Abstract Nanograined (grain size 6–15 nm) ZnO films
with various Fe content (between 0 and 40 at.%) were
synthesized by the novel liquid ceramics method. The films
with 0, 0.1, 5 and 10 at.% Fe contain only ZnO-based solid
solution with wurtzite structure. The films with 20 at.% Fe
contain mainly amorphous phase. The peaks of the second
phase ($ZnFe_2O_4$ with cubic lattice) become visible in the
X-ray diffraction spectra at 30 at.% Fe. Therefore, the
overall solubility of Fe in nanograined ZnO films at 550 °C
is about 20 at.% Fe. The solubility limit in the bulk is about
1.5 at.% Fe. The recently published papers on the structure
and magnetic behaviour of Fe-doped ZnO allowed us to
obtain the dependence of Fe solubility in ZnO on the grain
size. The overall Fe solubility drastically increases with the
decreasing grain size. The quantitative estimation shows
that, close to the bulk solubility limit, the thickness of a Fe-
enriched layer in grain boundaries is that of several
monolayers.

Introduction

The phase diagrams for the nanograined materials can
drastically differ from those for the single crystals or
coarse-grained polycrystals. For example, by increasing the
content of an alloying component, c, a solubility limit is
reached at a certain concentration, c_s. Above c_s, the second
phase appears in the bulk. Upon further increasing c, only
the amount of the second phase increases, but the con-
centration in the first phase remains equal to c_s. At $c > c_s$,
the diffraction peaks of a second phase appear in the X-ray
diffraction (XRD) spectrum, and in the electron diffraction
pattern in transmission electron microscopy (TEM). How-
ever, if the alloy contains surfaces and interfaces with
segregated second components, then the total concentration
of a second component, c_t, will be higher than the con-
centration in the bulk solid solution, c_v. The difference
between c_t and c_v would increase with an increasing spe-
cific area of surfaces and interfaces (i.e. with the decreasing
grain size). If the grain size is small enough, then the dif-
ference between c_t and c_v can become measurable. This is
due to the fact that XRD registers the diffraction only from
the bulk phases. The component segregated in the thin
surface or interface layers remains invisible for XRD. The
XRD peaks appear only in the case where the coherent-
scattering region is large enough (grain size around 5 nm
or larger). Simultaneously, XRD allows one to measure the
grain size using the peak width.

McLean was probably the first who mentioned that the
apparent solubility limit, c_{sa}, in the fine-grained materials

S. G. Protasova · B. B. Straumal · A. A. Mazilkin · B. Baretzky
Karlsruher Institut für Technologie, Institut für Nanotechnologie,
Hermann-von-Helmholtz-Platz 1,
76344 Eggenstein-Leopoldshafen, Germany

S. G. Protasova · B. B. Straumal (✉) · A. A. Mazilkin
Institute of Solid State Physics, Russian Academy of Sciences,
Ac. Ossipyan str. 2, 142432 Chernogolovka, Russia
e-mail: straumal@issp.ac.ru; straumal@mf.mpg.de

B. B. Straumal
Moscow Institute of Physics and Technology (State University),
Institutskii per. 9, 141700 Dolgoprudny, Russia

S. V. Stakhanova · P. B. Straumal
National University of Science and Technology, "MISIS", 4,
Leninsky pr., 119049 Moscow, Russia

P. B. Straumal
Institute of Metallurgy and Materials Science, Russian Academy
of Sciences, Leninsky Prospect 49, 117991 Moscow, Russia

will be higher than the volume solubility limit c_s [1]. He calculated this difference for the Fe–C system and grain size of 1 and 10 μm [1]. Beke et al. calculated the shift of miscibility gap due to the GB segregation depending on the number of GB layers [2, 3]. Experimentally, such shift was observed in the Pd–H system [4]. The increase of the total solubility with the decreasing grain size was observed for Ti and Y in alumina [5, 6] and for Y and Ca in TiO_2 [7, 8].

Nevertheless, the consistent XRD measurements of solubility shift $c_{sa} - c_s$ depending on grain size d are very time-consuming. Zinc oxide offers a good possibility for such successive investigations. ZnO is broadly used as a transparent, conducting oxide in the semiconductor thin film technology, as a material for varistors (doped by Bi_2O_3) and for gas sensors. Moreover, it is a promising material for future spintronics as a possible ferromagnetic semiconductor. In 2000, Dietl et al. theoretically predicted that ZnO doped by small amounts of 'magnetic' impurities like Mn or Co should possess the ferromagnetic properties [9]. This work triggered a boom of experimental and theoretical work [10, 11]. In the meantime, more than 2000 papers devoted to dilute magnetic semiconductors have been published. The ferromagnetic behaviour was found also in other oxides, carbides and nitrides [12–15]. Nevertheless, ferromagnetism in diluted doped ZnO is far from understood. The presence or the absence of ferromagnetism in doped ZnO critically depends on the synthesis method. Fortunately, these studies allow the dependence of $c_{sa} - c_s$ on the grain (particle) size d to be estimated.

Therefore, the goal of this work is threefold: (1) to measure the solubility shift $c_{sa} - c_s$ in nanograined ZnO manufactured by the novel liquid ceramics method; (2) to analyse the $c_{sa} - c_s$ dependence on the grain size in the broad interval of d using the published data on ZnO; and (3) to compare the influence of segregation in surfaces and interfaces on the shift $c_{sa} - c_s$.

Experimental

The Fe-doped ZnO thin films were deposited on the Al foils and NaCl single crystals by the novel liquid ceramics method. The substrates were dip-coated by the mixture of liquid organic acids with metallic ions and dried at 150 °C. Then, the deposited layers were oxidized in air at 550 °C. The resulting films were greenish and transparent. The film thickness was determined by electron-probe microanalysis (EPMA) and edge-on TEM and measured between 50 and 200 nm. The Fe contents in films were 0, 0.1, 5, 10, 20, 30 and 40 at.%. The zinc and iron contents in doped oxides were measured by atomic absorption spectroscopy on a Perkin-Elmer spectrometer and by EPMA on a Tescan Vega TS5130 MM microscope equipped with the Oxford Instruments LINK energy-dispersive spectrometer. TEM

investigations were carried out on a JEM-2100 microscope at an accelerating voltage of 200 kV. TEM was used to investigate the crystal structure of the film especially at the interface and to look for possible Fe clusters. TEM was also used to measure the grain size in pure and doped ZnO films. XRD data were obtained on Siemens diffractometer (Cu K_α radiation with $\lambda = 0.154184$ nm) with a secondary monochromator. Calculation of the grain size, d, was done using the angle dependence of the peak broadening [16].

Results and discussion

In Fig. 1, the bright-field and dark-field high-resolution electron micrographs are shown for the nanograined ZnO thin film with 0.1 at.% Fe. The electron diffraction pattern is shown in the inset; it contains only the ZnO wurtzite rings. The deposited ZnO film is dense, non-porous, nanograined, uniform, and non-textured. The grain sizes (measured using XRD and TEM) in the films are 15, 8 and 6 nm for 0.1, 5 and 10 at.% Fe, respectively. Iron is rather uniformly distributed in the samples. TEM demonstrates the absence of the inhomogeneity in the submicroscale (i.e. on the length scale of 100–1000 nm). It does not mean that the Fe content is the same everywhere in the nanoscale (i.e. inside the crystalline grains and in the intergranular areas, see discussion below). In Fig. 2, the XRD spectra are shown for the Fe-doped ZnO films with 0.1, 5, 10, 20, 30 and 40 at.% Fe. The crystalline quality of ZnO films doped by Fe is much worse in comparison to those doped by Mn or Co [17 and references therein]. It is so in spite of the fact that the pure ZnO films and films doped with Mn, Co and Fe were obtained with the same 'liquid ceramics'' method under the same conditions [17 and references therein]. Already the film with 0.1 at.% Fe contains a certain amount of amorphous phase (Fig. 2). The XRD spectra (Fig. 2) demonstrate that the amount of the amorphous phase increases with the increasing Fe content, and the films with 20 at.% Fe contain mainly amorphous phase. The crystallinity of films with 30 and 40 at.% Fe improves again. The wurtzite lines are visible in the pure ZnO film (ICPDS Card No. 36-1451) and in ZnO films with 0.1, 5 and 10 at.% Fe. The peaks of the second phase ($ZnFe_2O_4$ with cubic lattice [18, 19]) become visible in the XRD spectra at 30 at.% Fe. Therefore, the overall solubility of Fe in ZnO films at 550 °C with grain sizes in the range of 6–15 nm is about 20 at.% Fe. The solubility limit in the bulk c_s is about 1.5 at.% Fe at 550 °C [20]. It is important to underline that the amorphous phase disappears simultaneously with the appearance of $ZnFe_2O_4$ phase. Moreover, the samples with 30 and 40 at.% Fe do not contain any wurtzite lines of ZnO. In samples with high concentration of Co and Mn, the wurtzite ZnO coexists with
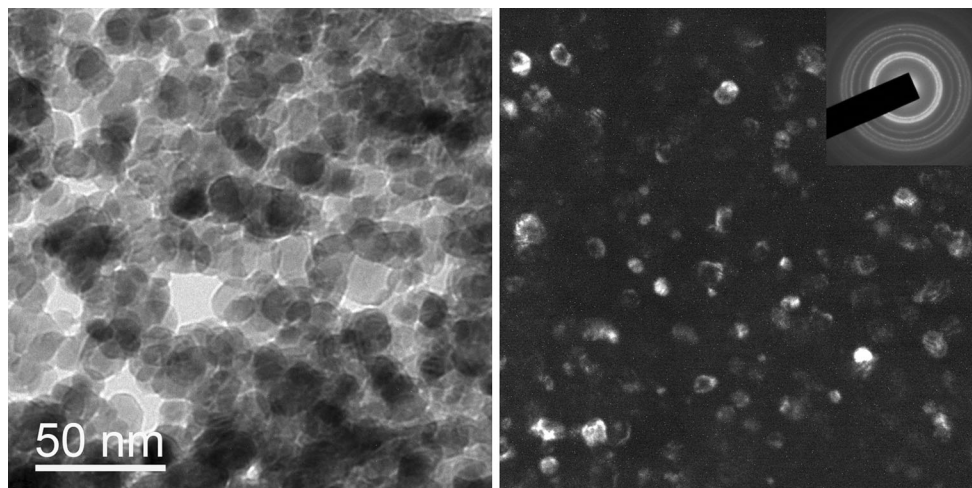
Fig. 1 Bright-field (*left*) and dark-field (*right*) high-resolution electron micrographs for the ZnO, 0.1 at.% Fe thin film. The electron diffraction pattern is shown in the *inset*
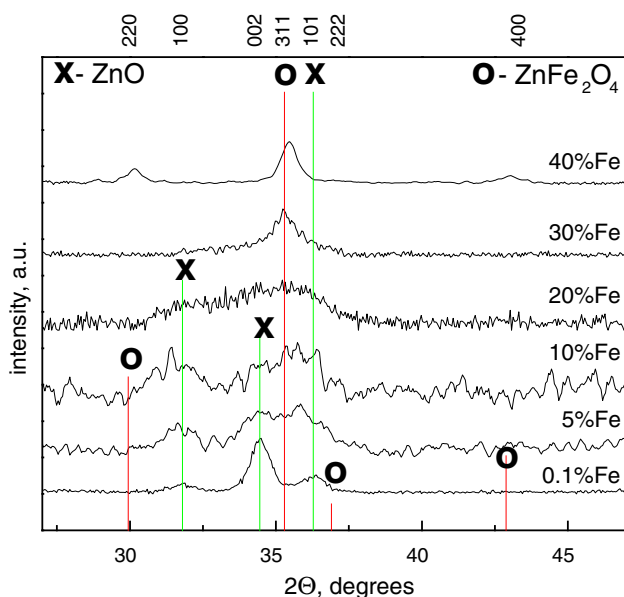

**Fig. 2** XRD spectra for the Fe-doped ZnO films with 0.1, 5, 10, 20, 30 and 40 at.% Fe

Mn_3O_4 or Co_2O_3 [17 and references therein]. The critical value of specific GB area s_{GB} needed for the ferromagnetic behaviour of Fe-doped ZnO is also unusually low [21] in comparison with Co-doped and Mn-doped ZnO [17 and references therein]. Pure ZnO also becomes ferromagnetic, but at very high s_{GB} (i.e. very fine grains) [22 and references therein]. The addition of 'magnetic' atoms indeed makes the transition to the ferromagnetic behaviour easier (as supposed by Dietl et al. [9]), but in another way, just by reduction of the needed amount of GBs [22]. Moreover, iron acts in a much more effective way than cobalt and manganese.

In order to find ferromagnetism in doped ZnO, it is important to ensure that it does not contain any particles of the second phase which could influence the sample's magnetic properties. In other words, it is essential that all the published articles include data on the dopant's concentration and the presence or the absence of the second phase. Usually, the presence or the absence of a second phase is controlled by XRD. In most cases, by means of the conventional experimental setup, the measurable X-ray peaks appear in the diffraction spectra when the amount of a second phase is about 5 %. It is known that TEM in the setup used by us allows one to detect a second phase at a much lower content, even less than 1 per cent, as was shown in Ref. [22 and references therein]. However, such TEM data are seldom present in the papers devoted to the magnetic behaviour of ZnO. Even more seldom are the high-precision XRD investigations for the formation of secondary $ZnFe_2O_4$ phase in Fe-doped ZnO [23]. The fact that the same method (conventional XRD) was used to control the presence of a second phase in Fe-doped ZnO allows us to compare the data from different works and to bring them together in the same plot.

The majority of published works allows us to estimate the grain or particle size and to assign the data to a certain temperature, either that of a synthesis or that of the last thermal treatment. The published data encompass a grain (particle) size D of between 1 mm and 10 nm and temperatures from 300 to 1500 K. This gave us the unique chance to construct the $c_{sa}(T)$ dependences for the broad interval of D and to compare the influences of internal boundaries and surfaces. The largest data arrays exist for Co-, Fe- and Mn-doped ZnO. The data for Co- and Mn-doped ZnO have been analysed earlier [22 and references therein]. In this work, we will analyse the Fe-doped ZnO.
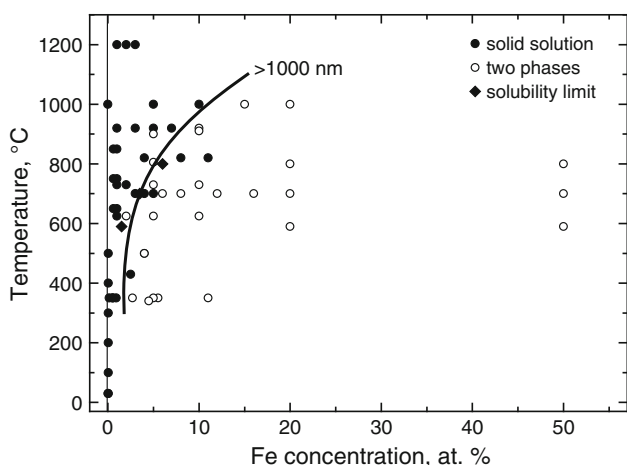
Fig. 3 Solubility limit of Fe in ZnO polycrystals with grain sizes >1000 nm [20, 24–43]
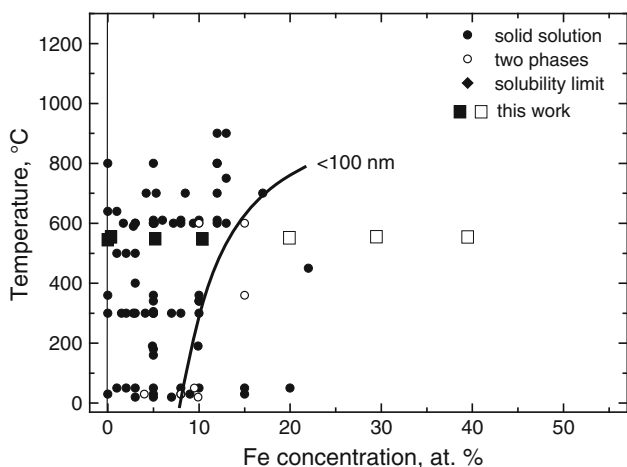

Fig. 4 Solubility limit of Fe in ZnO polycrystals with grain sizes below 100 nm [44–72]

In Fig. 3, the solubility (solvus) limit of Fe in ZnO polycrystals is drawn using the data on polycrystals with grain a size of >1000 nm [20, 24–43]. The errors in Fig. 3, as well as in Fig. 4 are less than the scales of the markers. These samples were obtained by hydrothermal growth [20, 24], sintering of conventional powders [25–31], chemical vapor transport [32], Fe ion implantation into ZnO single crystals [33–41], ball milling [42] and CVD [43]. The solubility of Fe in ZnO reaches about 10 at.% at 1000 °C and falls to 1–1.5 at.% at 400 °C. This line corresponds to the solubility in the volume of ZnO, and the number of Fe atoms segregated in grain boundaries is negligible.

In Fig. 4, the solubility limit (solvus) of Fe in ZnO polycrystals is drawn using the data on polycrystals with grain size <100 nm [44–72]. These samples were obtained by the wet chemistry deposition methods (including sol–

gel method) [44–51], magnetron sputter deposition [52–57], pulsed laser deposition (PLD) [58–60], CVD [61], Fe ion implantation into thin films [62], chemical pyrophoric reaction process [63–65], mechanical alloying [66, 67], electro-codeposition of nanowires [68], hydrolysis of metallic powders [69], and co-precipitation or sintering of nanopowders [70–72]. The data obtained in this work are shown by the large circles. For the estimation of the grain sizes in case of porous samples or non-equiaxial (flattened or elongated) grains, we applied the procedure used earlier for the calculation of specific GB area s_{GB} needed for the description of ferromagnetic behaviour of Fe-doped ZnO [21]. In other words, we introduced the additional porosity coefficient, p. p varies from 0 for the nonsintered powders to 1 for the fully compacted polycrystals. We estimated p values using the published micrographs. In many cases, the samples were poreless; however, the grains were not equiaxial but elongated or flattened. In these cases, we used the aspect ratio a (ratio of grain width to grain height). For the flattened grains, $a > 1$; and for the elongated ones, $a < 1$. The solubility of Fe in ZnO (for $D < 100$ nm) reaches about 25 at.% at 700 °C and falls to <5 at.% at room temperature. Fe solubility in polycrystals with grain size <100 nm is much higher than in the coarse-grained samples. For example, at 600 °C, it is ten times higher.

Based on the knowledge that Fe solubility depends on grain size (Figs. 3, 4), it is possible to estimate the maximum Fe segregation in ZnO GBs. Let us calculate first the area-to-volume ratio for the grains and particles. If we suppose that grains and particles are spheres with diameter D, then the surface area for each particle is πD^2, and the GB area for each grain is $\pi D^2/2$ (since each GB is shared between two neighbouring grains). The volumes for spherical grains and particles are the same, namely, $\pi D^3/6$. Thus, the area-to-volume ratio, A, for the free surfaces of spherical particles is $A_{FS} = 3/D$, and for GBs of spherical grains, $A_{GB} = 3/2D$. One of the earliest studies of grain shape was made by Lord Kelvin in 1887 [73]. According to his work, the grain shape for optimal space-filling, is a polyhedron known as a tetrakaidecahedron. It has 14 faces, 24 corners and 36 edges. Tetrakaidecahedrons ensure a minimal surface area and surface tension. Tetrakaidecahedron is an octahedron truncated by cube. The ratio of tetrakaidecahedron's surface area to that of a sphere of the same volume is 1.099 [73]. Thus, the area-to-volume ratio for polyhedral grains is $A_{GB} = 1.65/D$. If the ZnO free surfaces or GBs are covered by one monolayer (ML) of Fe covers, then one can calculate their input, c_{FS} or c_{GB}, in the full concentration as a product of the thickness, t, of a surface or GB layer and A_{FS} or A_{GB}. One can estimate the lattice constant of ZnO wurtzite lattice d as the cubic root from the unit cell volume. According to our measurements, the unit cell volume for ZnO is about 47×10^{-3} nm³.
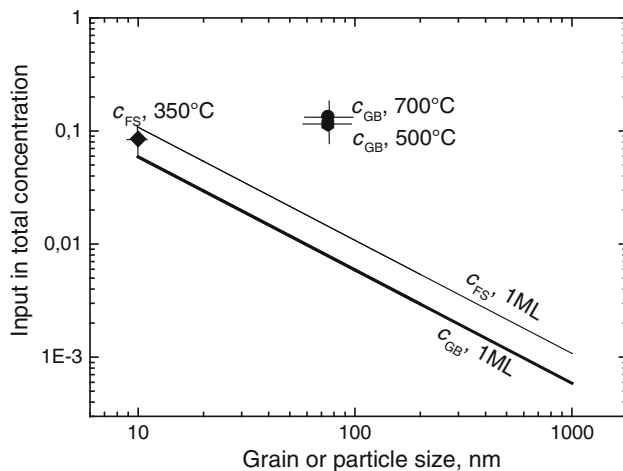
Fig. 5 Size dependence of the input of GB or surface Fe segregation into full Fe content

Therefore, $d = 0.36$ nm. Thus, for the one monolayer, $t = d$; $c_{FS} = dA_{FS} = 1.08/D$; and $c_{GB} = d A_{GB} = 0.59/D$.

In Fig. 5, the inputs of Fe accumulated in GBs and surfaces in total concentration are shown for different grain sizes. c_{FS} and c_{GB} values for 1 ML are shown by thin and thick straight lines, respectively, with a slope of –1 in the bottom part of the Fig. 5. The solubility limits of Fe in the single-crystalline or coarse-grained ZnO at 500 and 700 °C are 1.8 and 3.4 at.% Fe, respectively (Fig. 3). If we subtract these values from the solubility limit of Fe in the fine-grained ZnO (Fig. 4), then we obtain the GB input, c_{GB}, into total Fe solubility in the ZnO polycrystals. The c_{GB} values are shown in Fig. 5 by full circle (700 °C) and full hexagon (500 °C). The solubility limit of Fe in the single-crystalline or coarse-grained ZnO at 350 °C is equal to 1.4 at.% Fe (Fig. 3). The solubility limit in the fine-grained powder (particle size) synthesized at 350 °C using the chemical pyrophoric reaction method is about 10 at.% Fe [65]. The respective free surface segregation values, c_{FS}, are shown in Fig. 5 by full diamond. It is easy to see that the experimental c_{GB} values are higher than the calculated values for 1 ML by more than one order of magnitude. This fact undoubtedly indicates the multilayer GB Fe segregation in ZnO. The c_{FS} point for free surfaces (full diamond) lies less than the c_{GB} values for GBs and nearly coincide with the calculated value for 1 ML in the surface. It means that free surfaces can accumulate much less Fe in comparison with GBs and do not reveal the multilayer Fe adsorption. Thus, the behaviour of Fe atoms in the ZnO free surfaces is quite different from those of Co and Mn GBs [22 and references therein]. In other words, the ZnO-free surfaces contain about 2-4 ML of Co and Mn. The Fe-enriched ZnO surfaces contain the conventional single-layer McLean segregation.

Figure 5 undoubtedly indicates that the Fe enrichment of GBs in the fine-grained ZnO cannot be reduced to the simple single-layer GB segregation analysed by McLean [1]. It is also very similar to the behaviours of Co and Mn in ZnO GBs [22 and references therein]. The GB phase of a finite thickness of a few nm was first observed in the pioneering works of David A. Clarke on silicon nitride [74–77]. He theoretically treated the GB phase with the aid of force–balance model. Later, nanometre-thick (nm-thick), disordered films of a nearly constant thickness have been frequently observed in oxide/metal interfaces [78–80] and GBs in ceramics [75–77, 81–90]. Thin equilibrium surface films were first considered by Cahn [91]. He predicted the possible existence of such films in the one-phase area of a bulk phase diagram. Cahn proposed the idea that the transition from incomplete to complete surface wetting is a true phase transformation. Later, this idea was successfully applied for GBs, and also old data on GB wetting were reconsidered from this point of view [92, 93]. Especially informative were the experiments with single GBs in bicrystals [93–95]. GB wetting-phase transformation proceeds at the temperature T_{wGB} where GB energy σ_{GB} becomes equal to the energy $2\sigma_{SL}$ of two solid/liquid interfaces. Above T_{wGB}, GB is substituted by a layer of the melt. The tie-line of the GB wetting phase transition in the two-phase area of a bulk phase diagram can continue into the one-phase area. It is called then a GB solidus (or prewetting) line. GB contains the thin layer of a GB phase between GB solidus and bulk solidus lines. Above T_{wGB}, the energy gain ($\sigma_{GB} - 2\sigma_{SL}$) permits such a thin layer of a GB phase to stabilize between the abutting crystals. Such GB phase is metastable in the bulk and becomes stable in the GB. The formation of metastable phase layer of thickness l leads to the energy loss $l\Delta g$. The equality of the energy gain ($\sigma_{GB} - 2\sigma_{SL}$) and energy loss $l\Delta g$ defines the finite thickness l of the GB phase. In this simplest model, the prewetting GB layer of finite thickness l suddenly appears if one intersects the GB soludus (prewetting or premelting) line $c_{bt}(T)$. Thickness l logarithmically diverges close to the line of bulk solidus. It is because from the thermodynamic pint of view, the thickness of a wetting phase is infinite in the two-phase area of a phase diagram. Physically, in the two-phase area, the thickness of wetted GB is defined only by the amount of the wetting phase. The direct HREM evidence for thin GB films and triple junction 'pockets' of liquid-like phase have been recently obtained in metallic Al–Zn [96, 97] and W–Ni [98, 99] alloys.

Later, these ideas were generalized and developed further [100–104]. Most probably in the nanograined ZnO–FeO polycrystals (as well as in Co- and Mn-doped ZnO [22 and references therein]), the situation is more complicated than that in the simple sequence 'monolayer adsorption → interfacial film → macroscopically thick complete

wetting film'. Additional complexity comes from the possible GB layering, GB roughening, pseudo-partial (or frustrated-complete) melting/wetting, first-order or continuous adsorption/wetting transitions and interfacial critical points [100–104]. The nm-thick GB films have been observed in ZnO doped by Bi_2O_3 [81, 82, 105–113]. ZnO doped by Bi is used for manufacturing of varistors. These devices exhibit highly nonlinear current–voltage characteristics. They possess a high resistivity below a threshold electric field and become conductive when this field is exceeded. This phenomenon enables them to be used in the current over-surge-protection circuits [112, 113]. After liquid-phase sintering, such material consists of ZnO grains separated by thin Bi_2O_3-rich GB layers. Interfaces between ZnO grains determine the nonlinear current–voltage characteristics. The GB wetting-phase transformation governs the presence of a few nm-thick Bi-rich GB phase in ZnO. The more complicated situation was also observed in the ZnO–Bi_2O_3 system, namely, during the transition from pseudo-partially wetted GBs to the completely wetted ones [105]. In this case, the Bi_2O_3 droplets having non-zero contact angle in the GB plane may exist in the equilibrium with thin GB layer.

The reason for the high value of GB thickness obtained from Fig. 5 may be the logarithmic divergence of the GB layer's thickness predicted by Cahn's model. We calculated the data for the points in Fig. 5 based on the apparent shift of the total solubility of Fe. It means that the calculated GB thickness corresponds to that at the solubility (solvus) line. The few nm-thick Bi-rich layers were observed also in the ZnO surfaces [114–116]. Their thicknesses were close to those of GB layers [105–107]. The thicknesses of surficial films were explained by the pseudo-partial (frustrated-complete) surface wetting [105, 116]. In case of the pseudo-partial wetting, the thickness of a surficial (or GB) film also increases with the increasing dopant's concentration (activity) and can reach that of a few monolayers. However, it does not diverge, and remains finite by approaching the solubility limit line [104, 114, 117]. In the case of Fe-doped ZnO, the estimation presented in Fig. 5 predicts lower Fe-capacity of free surfaces in comparison with GBs. This fact has to be carefully investigated in the future experiments. We observed recently that the ferromagnetic behaviour in pure ZnO critically depends on the amorphous interlayers between ZnO nanograins [22 and references therein]. Even in the case of undoped ZnO, these GB layers are rather thick. The doping of ZnO with Co, Mn or Fe [21, 22 and references therein] non-trivially influences the saturation magnetization of doped ZnO. Most probably, the non-monotonous dependences of saturation magnetization on dopant's concentration correlate with the variety of possible valence states of Co, Fe or Mn [22 and references therein].

Therefore, based on the results obtained in this work, one can expect to observe in the future, various interesting GB phases and phase transformations in the Fe-doped ZnO. Furthermore, the observed shift of the solvus line in the Fe-doped ZnO will also permit one to explain the mysterious phenomenon of the room-temperature ferromagnetism in the broad-band transparent semiconductor ZnO.

Conclusions

1. The accumulation of Fe in grain boundaries and free surfaces drastically shifts the line of Fe solubility limit in ZnO to the higher Fe concentrations. For example, at 550 °C, the total solubility in the bulk is about 1.5 at.% Fe, and in the nanograined sample with grain size <10 nm, it is about 20 at.% Fe.

2. Small grain size leads to the larger shift compared to similarly small particle sizes. This means that the Fe accumulation ability of grain boundaries is about 10 times higher than that of free surfaces.

3. Thus, the phase diagrams for the materials having a grain size <1000 nm have to be investigated in a fresh study. An especially drastic change to the phase diagrams results when the grain size is <100 nm.

References

1. McLean D (1957) Grain boundaries in metals. Clarendon Press, Oxford
2. Beke DL, Cserháti C, Erdélyi Z, Szabó IA (2002) Segregation in nanostructures. In: Nalwa HS (ed) Nanoclusters and nanocrystals. American Scientific Publishers, Valencia
3. Beke DL, Erdélyi Z, Bakos P, Cserháti C, Szabó IA (1999) Segregation induced phase transformations in nanostructures. In: Koiwa M, Otsuka K, Miyazaki T (eds) Proceedings of the international conference solid–solid phase transformations'99 (JIMIC-3). The Japan Inst. Met., Tokyo
4. Weissmuller J, Chr L (2000) On the size dependence of the critical point of nanoscale interstitial solid solutions. Philos Mag Lett 80:411–418
5. Lartigue-Korinek S, Legros C, Carry C, Herbst F (2006) Titanium effect on phase transformation and sintering behavior of transition alumina. J Eur Ceram Soc 26:2219–2230
6. Gülgün MA, Voytovych R, Maclaren I, Rühle M, Cannon RM (2002) Cation segregation in an oxide ceramic with low solubility: yttrium doped alpha-alumina. Interface Sci 10:99–110
7. Wang Q, Lian G, Dickey EC (2004) Grain boundary segregation in yttrium-doped polycrystalline TiO_2. Acta Mater 52:809–820
8. Terwilliger CD, Chiang YM (1995) Size-dependent solute segregation and total solubility in ultrafine polycrystals: Ca in TiO_2. Acta Metall Mater 43:319–328

9. Dietl T, Ohno H, Matsukura F, Cibert J, Ferrand D (2000) Zener model description of ferromagnetism in zinc-blended magnetic semiconductors. Science 287:1019–1022

10. Dietl T (2010) A ten-year perspective on dilute magnetic semiconductors and oxides. Nat Mater 9:965–974

11. Sato K, Katayama-Yoshida H (2002) First principles materials design for semiconductor spintronics. Semicond Sci Technol 17:367–376

12. Cheng FF, Ding BF, Pan F, Yao SD, Potzger K, Zhou SQ (2012) Investigation on the structural and magnetic properties of Co^+ implanted rutile TiO_2. Nucl Instrum Methods Phys Res B 286:180–183

13. Prucnal S, Shalimov A, Ozerov M, Potzger K, Skorupa W (2012) Magnetic and optical properties of virgin arc furnace grown MgO crystals. J Cryst Growth 339:70–74

14. Potzger K (2012) Ion-beam synthesis of magnetic semiconductors. Nucl Instrum Methods Phys Res B 272:78–87

15. Ding BF, Cheng FF, Pan F, Fa T, Yao S, Potzger K, Zhou SQ (2012) The correlation between structure and magnetism of Ni-implanted TiO_2 annealed at different temperatures. J Magn Magn Mater 324:33–36

16. Soyer A (1993) LMCTEP: software for crystal-structure representation. J Appl Crystallogr 26:495

17. Straumal BB, Mazilkin AA, Protasova SG, Straumal PB, Myatiev AA, Schütz G, Goering E, Tietze Th, Baretzky B (2013) Grain boundaries as the controlling factor for the ferromagnetic behaviour of Co-doped ZnO. Philos Mag 93:1371–1383

18. König U, Chol G (1968) Röntgenbeugungs- und Neutronenbeugungsuntersuchungen an Ferriten der reihe Mn_x-$Zn_{1-x}Fe_2O_4$. J Appl Crystallogr 1:124–128

19. Zhou S, Potzger K, Reuther H, Talut G, Eichhorn F, von Borany J, Skorupa W, Helm M, Fassbender J (2007) Crystallographically oriented magnetic $ZnFe_2O_4$ nanoparticles synthesized by Fe implantation into ZnO. J Phys D 40:964–969

20. Bates CH, White WB, Roy R (1966) The solubility of transition metal oxides in zinc oxide and the reflectance spectra of Mn^{2+} and Fe^{2+} in tetrahedral fields. J Inorg Nucl Chem 28:397–405

21. Straumal BB, Protasova SG, Mazilkin AA, Straumal PB, Schütz G, Tietze Th, Goering E, Baretzky B (2013) Ferromagnetic behaviour of Fe-doped ZnO nanograined films. Beilstein J Nanotechnol 4:361–369

22. Straumal BB, Protasova SG, Mazilkin AA, Schütz G, Goering E, Baretzky B, Straumal PB (2013) Ferromagnetism of zinc oxide nanograined films. JETP Lett 97:367–377

23. Zhou S, Potzger K, Reuther H, Talut G, von Borany J, Skorupa W, Helm M, Fassbender J (2008) Using X-ray diffraction to identify precipitates in transition metal doped semiconductors. J Appl Phys 103:07D530

24. Zhang H-W, Wei Z-R, Li Z-Q, Dong G-Y (2007) Room-temperature ferromagnetism in Fe-doped, Fe- and Cu-codoped ZnO diluted magnetic semiconductor. Mater Lett 61:3605–3607

25. Kolesnik S, Dabrowski B, Mais J (2004) Structural and magnetic properties of transition metal substituted ZnO. J Appl Phys 95:2582–2586

26. Shim JH, Hwang T, Lee S, Park JH, Han S-J, Jeong JH (2005) Origin of ferromagnetism in Fe- and Cu-codoped ZnO. Appl Phys Lett 86:082503

27. Blasco J, Bartolomé F, García LM, García J (2006) Extrinsic origin of ferromagnetism in doped ZnO. J Mater Chem 16:2282–2288

28. Han S-J, Song JW, Yang C-H, Park SH, Park J-H, Jeong YH, Rhie KW (2002) A key to room-temperature ferromagnetism in Fe-doped ZnO:Cu. Appl Phys Lett 81:4212–4214

29. Blasco J, Bartolomé F, García LM, García J (2007) Magnetic properties of doped ZnO prepared by different synthetic routes. J Magn Magn Mater 316:e177–e180

30. Jayakumar OD, Gopalakrishnan IK, Kulshreshtha SK (2006) Magnetization study of Fe-doped ZnO co-doped with Cu: synthesized by wet chemical method. J Mater Sci 41:4706–4712. doi:10.1007/s10853-006-0045-4

31. Ahn GY, Park S-I, Shim I-B, Kim CS (2004) Mössbauer studies of ferromagnetism in Fe-doped ZnO magnetic semiconductor. J Magn Magn Mater 282:166–169

32. Tamura T, Ozaki H (2009) The relationship of the magnetic properties of M (M = Mn, Fe, Co)-doped ZnO single crystals and their electronic structures. J Phys Condens Matter 21:026009

33. Zhou S, Potzger K, Talut G, Reuther H, von Borany J, Grötzschel R, Skorupa W, Helm M, Fassbender J (2008) Fe-implanted ZnO: magnetic precipitates versus dilution. J Appl Phys 103:023902

34. Weyer G, Gunnlaugsson HP, Mantovan R, Fanciulli M, Naidoo D, Bharuth-Ram K, Agne T (2007) Defect-related local magnetism at dilute Fe atoms in ion-implanted ZnO. J Appl Phys 102:113915

35. Polyakov AY, Govorkov AV, Smirnov NB, Pashkova NV, Pearton SJ, Ip K, Frazier RM, Abernathy CR, Norton DP, Zavada JM, Wilson RG (2004) Optical and magnetic properties of ZnO bulk crystals implanted with Cr and Fe. Mater Sci Semicond Proc 7:77–81

36. Wang D, Chen ZQ, Zhou F, Lu W, Maekawa M, Kawasuso A (2009) Ferromagnetism and microstructure in Fe^+-implanted ZnO. Appl Surf Sci 255:9371–9375

37. Schumm M, Koerdel M, Müller S, Ronning C, Dynowska E, Gołacki Z, Szuszkiewicz W, Geurts J (2009) Secondary phase segregation in heavily transition metal implanted ZnO. J Appl Phys 105:083525

38. Zhou S, Potzger K, Xu Q, Talut G, Lorenz M, Skorupa W, Helm M, Fassbender J, Grundmann M, Schmidt H (2009) Ferromagnetic transition metal implanted ZnO: a diluted magnetic semiconductor? Vacuum 83:S13–S19

39. Wu P, Saraf G, Lu Y, Hill DH, Gateau R, Wielunski L, Bartynski RA, Arena DA, Dvorak J, Moodenbaugh A, Siegrist T, Raley JA, Yeo YK (2006) Ferromagnetism in Fe-implanted a-plane ZnO films. Appl Phys Lett 89:012508

40. Potzger K, Zhou S, Reuther H, Mücklich A, Eichhorn F, Schell N, Skorupa W, Helm M, Fassbender J, Herrmannsdörfer T, Papageorgiou TP (2006) Fe implanted ferromagnetic ZnO. Appl Phys Lett 88:052508

41. Rita E, Wahl U, Correia JG, Alves E, Soares JC (2004) Lattice location and thermal stability of implanted Fe in ZnO. Appl Phys Lett 85:4899–4901

42. Karamat S, Ke C, Tan TL, Zhou W, Lee P, Rawat RS (2009) Investigation of impurity phase formation for $ZnO_{1-x}TMO_x$ bulk samples formed by ball milling. Appl Surf Sci 255:4814–4820

43. Chen J, Liu J, West A, Yan Y, Yu M, Zhou W (2008) Room temperature ferromagnetism of FeCo-codoped ZnO nanorods prepared by chemical vapor deposition. IEEE Trans Magn 44:2681–2683

44. Shinagawa T, Izaki M, Inui H, Murase K, Awakura Y (2006) Microstructures and MR effects of transparent ferromagnetic chemically prepared Fe–Zn–O films. Phys Stat Sol A 203:2760–2764

45. Liu H, Yang J, Zhang Y, Wang Y, Wei M (2008) Ferromagnetism and exchange bias in Fe-doped ZnO nanocrystals. Mater Chem Phys 112:1021–1023

46. Zhang B, Li QH, Shi LQ, Cheng HS, Wang JZ (2008) Room temperature ferromagnetism of Fe-implanted ZnO film. J Vac Sci Technol A 26:1469–1473

47. Zhang Y, Wu L, Li H, Xu J, Han L, Wang B, Tuo Z, Xie E (2009) Influence of Fe doping on the optical property of ZnO films. J Alloys Compd 473:319–322

48. Liu H, Yang J, Zhang Y, Yang L, Wei M, Ding X (2009) Structure and magnetic properties of Fe-doped ZnO prepared by the sol–gel method. J Phys Condens Matter 21:145803

49. Yoon SW, Cho S-B, We SC, Yoon S, Suh BJ, Song HK, Shin YJ (2003) Magnetic properties of ZnO-based diluted magnetic semiconductors. J Appl Phys 93:7879–7881

50. Glaspell G, Dutta P, Manivannan A (2005) A room-temperature and microwave synthesis of M-doped ZnO (M = Co, Cr, Fe, Mn & Ni). J Cluster Sci 16:523–536

51. Fernandes DM, Winkler Hechenleitner AA, Silva MF, Lima MK, Stival Bittencourt PR, Silva R, Custydio Melo MA, Gymez Pineda EA (2009) Preparation and characterization of NiO, Fe_2O_3, $Ni_{0.04}Zn_{0.96}O$ and $Fe_{0.03}Zn_{0.97}O$ nanoparticles. Mater Chem Phys 118:447–452

52. Cho YM, Choo WK, Kim H, Kim D, Ihm YE (2002) Effects of rapid thermal annealing on the ferromagnetic properties of sputtered $Zn_{1-x}(Co_{0.5}Fe_{0.5})_xO$ thin films. Appl Phys Lett 80:3358–3360

53. Seo SY, Kwak CH, Lee YB, Kim SH, Park SH, Han SW (2008) Structural and magnetic properties of $Zn_{1-x}Fe_xO$ thin films synthesized by RF magnetron sputtering. J Korean Phys Soc 52:805–809

54. Seo SY, Kwak CH, Lee YB, Kim SH, Park SH, Han SW (2008) Hole-induced ferromagnetic properties of Fe-added ZnO films. J Korean Phys Soc 52:249–252

55. Chen AJ, Wu XM, Sha ZD, Zhuge LJ, Meng YD (2006) Structure and photoluminescence properties of Fe-doped ZnO thin films. J Phys D 39:4762–4765

56. Wang C, Chen Z, He Y, Li L, Zhang D (2009) Structure, morphology and properties of Fe-doped ZnO films prepared by facing-target magnetron sputtering system. Appl Surf Sci 255:6881–6887

57. Zhao RB, Hou DL, Wei YY, Zhou ZZ, Pan CF, Zhen CM, Tang GD (2009) Ferromagnetism in Fe-doped ZnO thin films. Mod Phys Lett B 23:815–824

58. Dorneles LS, O'Mahony D, Fitzgerald CB, McGee F, Venkatesan M, Stanca I, Lunney JG, Coey JMD (2005) Structural and compositional analysis of transition-metal-doped ZnO and GaNPLD thin films. Appl Surf Sci 248:406–410

59. Venkatesan M, Fitzgerald CB, Lunney JG, Coey JMD (2004) Anisotropic ferromagnetism in substituted zinc oxide. Phys Rev Lett 93:177206

60. Hong NH, Sakai J, Brizé V (2007) Observation of ferromagnetism at room temperature in ZnO thin films. J Phys Condens Matter 19:036219

61. Feng QJ, Shen DZ, Zhang JY, Li BH, Zhang ZZ, Lu YM, Fan XW (2008) Room temperature ferromagnetic properties of ZnFeO thin films prepared by thermal oxidation of ZnFeS thin films. Mater Mater Chem Phys 112:1106–1109

62. Kumar R, Pratap Singh A, Thakur P, Chae KH, Choi WK, Angadi B, Kaushik SD, Patnaik S (2008) Ferromagnetism and metal-semiconducting transition in Fe-doped ZnO thin films. J Phys D Appl Phys 41:155002

63. Mandal SK, Nath TK, Karmakar D (2008) Magnetic and optical properties of $Zn_{1-x}Fe_xO$ (x = 0.05 and 0.10) diluted magnetic semiconducting nanoparticles Philos Mag 88:265–275

64. Kataoka T, Kobayashi M, Song GS, Sakamoto Y, Fujimori A, Chang FH, Lin HJ, Huang DJ, Chen CT, Mandal SK, Nath TK, Karmakar D, Dasgupta I (2009) X-ray magnetic circular dichroism investigations of the origin of room temperature ferromagnetism in Fe-doped ZnO nanoparticles. Jpn J Appl Phys 48:04C200

65. Karmakar D, Mandal SK, Kadam RM, Paulose PL, Rajarajan AK, Nath TK, Das AK, Dasgupta I, Das GP (2007) Ferromagnetism in Fe-doped ZnO nanocrystals: experiment and theory. Phys Rev B 75:144404

66. Kimishima Y, Uehara M, Irie K, Ishihara S, Yamaguchi Y, Saitoh TM, Kimoto K, Matsui Y (2008) Production of bulk dilute ferromagnetic semiconductor by mechanical milling. J Magn Magn Mater 320:e674–e677

67. Lin Y, Jiang D, Lin F, Shi W, Ma X (2007) Fe-doped ZnO magnetic semiconductor by mechanical alloying. J Alloys Compd 436:30–33

68. Xin M, Chen Y, Jia C, Zhang X (2008) Electro-codeposition synthesis and room temperature ferromagnetic anisotropy of high concentration Fe-doped ZnO nanowire arrays. Mater Lett 62:2717–2720

69. Uum YR, Han BS, Lee HM, Hong SM, Kim GM, Rhee CK (2007) Magnetic and photocatalytic effect of Fe-doped nano-rod ZnO synthesized by the hydrolysis of metal powders. Phys Stat Sol C 4:4408–4411

70. Alaria J, Venkatesan M, Coey JMD (2008) Magnetism of ZnO nanoparticles doped with 3d cations prepared by a solvothermal method. J Appl Phys 103:07D123

71. Rattana T, Suwanboon S, Amornpitoksuk P, Haidoux A, Limsuwan P (2009) Improvement of optical properties of nanocrystalline Fe-doped ZnO powders through precipitation method from citrate-modified zinc nitrate solution. J Alloys Compd 480:603–607

72. Sharma PK, Dutta RK, Pandey AC, Layek S, Verma HC (2009) Effect of iron doping concentration on magnetic properties of ZnO nanoparticles. J Magn Magn Mater 321:2587–2591

73. Hosford WF (2007) Materials science: an intermediate text. Cambridge University Press, Cambridge

74. Clarke DR (1987) On the equilibrium thickness of intergranular glass phases in ceramic materials. J Am Ceram Soc 70:15–22

75. Clarke DR, Shaw TM, Philipse AP, Horn RG (1993) Possible electrical double-layer contribution to the equilibrium thickness of intergranular glass-films in polycrystalline ceramics. J Am Ceram Soc 76:1201–1204

76. Tanaka I, Kleebe HJ, Cinibulk MK, Bruley J, Clarke DR, Rühle MJ (1994) Calcium concentration dependence of the intergranular film thickness in silicon. Am Ceram Soc 77:911–914

77. Bobeth M, Clarke DR, Pompe W (1999) A diffuse interface description of intergranular films in polycrystalline ceramics. J Am Ceram Soc 82:1537–1546

78. Avishai A, Scheu C, Kaplan WD (2005) Intergranular films at metal–ceramic interfaces Part I—interface structure and chemistry. Acta Mater 53:1559–1569

79. Levi G, Kaplan WD (2006) The influence of interfacial wetting and adhesion on the formation of voids at metal-ceramic interfaces. J Mater Sci 41:817–821. doi:10.1007/s10853-006-6565-0

80. Baram M, Kaplan WD (2006) Intergranular films at Au-sapphire interfaces. J Mater Sci 41:7775–7784. doi:10.1007/s10853-006-0897-7

81. Lee JR, Chiang YM, Ceder G (1997) Pressure-thermodynamic study of grain boundaries: Bi segregation in ZnO. Acta Mater 45:1247–1257

82. Wang H, Chiang YM (1998) Thermodynamic stability of intergranular amorphous films in bismuth-doped zinc oxide. J Am Ceram Soc 81:89–96

83. Kleebe HJ, Hoffmann MJ, Rühle M (1992) Influence of secondary phase chemistry on grain boundary film thickness in silicon nitride. Z Metallkd 83:610–617

84. Kleebe HJ, Cinibulk MK, Cannon RM, Rühle M (1993) Statistical analysis of the intergranular film thickness in silicon nitride ceramics. J Am Ceram Soc 76:1969–1977

85. Chiang YM, Silverman LA, French RH, Cannon RM (1994) Thin glass film between ultrafine conductor particles in thick-film resistors. J Am Ceram Soc 77:1143–1152

86. Ackler HD, Chiang YM (1997) Model experiment on thermodynamic stability of retained intergranular amorphous films. J Am Ceram Soc 80:1893–1896

87. Chiang YM, Wang H, Lee JR (1998) HREM and STEM of intergranular films at zinc oxide varistor grain boundaries. J Microsc 191:275–285

88. Ackler HD, Chiang YM (1999) Effect of initial microstructure on final intergranular phase distribution in liquid-phase-sintered ceramics. J Am Ceram Soc 82:183–189

89. Cannon RM, Esposito L (1999) High temperature colloidal behavior: particles in liquid silicates. Z Metallkd 90:1002–1015

90. Luo J, Wang H, Chiang YM (1999) Origin of solid-state activated sintering in Bi_2O_3-doped ZnO. J Am Ceram Soc 82:916–920

91. Cahn JW (1977) Critical point wetting. J Chem Phys 66:3667–3672

92. Eustathopoulos N (1983) Energetics of solid/liquid interfaces of metals and alloys. Int Met Rev 28:189–210

93. Straumal BB, Gust W, Watanabe T (1999) Tie lines of the grain boundary wetting phase transition in the Zn-rich part of the Zn–Sn phase diagram. Mater Sci Forum 294(296):411–414

94. Semenov VN, Straumal BB, Glebovsky VG, Gust W (1995) Preparation of Fe–Si single crystals and bicrystals for diffusion experiments by the electron-beam floating zone technique. J Cryst Growth 151:180–186

95. Straumal B, Rabkin E, Lojkowski W, Gust W, Shvindlerman LS (1997) Pressure influence on the grain boundary wetting phase transition in Fe–Si alloys. Acta Mater 45:1931–1940

96. Straumal BB, Mazilkin AA, Kogtenkova OA, Protasova SG, Baretzky B (2007) Grain boundary phase observed in Al-5 at.% Zn alloy by using HREM. Philos Mag Lett 87:423–430

97. Straumal BB, Kogtenkova O, Zięba P (2008) Wetting transition of grain-boundary triple junctions. Acta Mater 56:925–933

98. Gupta VK, Yoon DH, Meyer HM III, Luo J (2007) Thin intergranular films and solid-state activated sintering in nickel-doped tungsten. Acta Mater 55:3131–3142

99. Luo J, Gupta VK, Yoon DH, Meyer HM (2005) Segregation-induced grain boundary premelting in nickel-doped tungsten. Appl Phys Lett 87:231902

100. Tang M, Carter WC, Cannon RM (2006) Grain boundary transitions in binary alloys. Phys Rev Lett 97:075502

101. Tang M, Carter WC, Cannon RM (2006) Diffuse interface model for structural transitions of grain boundaries. Phys Rev B 73:024102

102. Luo J, Tang M, Cannon RM, Carter WC, Chiang YM (2006) Pressure-balance and diffuse-interface models for surficial amorphous films. Mater Sci Eng A 422:19–28

103. Kaplan WD, Chatain D, Wynblatt P, Carter WC (2013) A review of wetting versus adsorption, complexions, and related phenomena: the rosetta stone of wetting. J Mater Sci 48:5681–5717. doi:10.1007/s10853-013-7462-y

104. Luo J (2007) Stabilization of nanoscale quasi-liquid interfacial films in inorganic materials: a review and critical assessment. Crit Rev Solid State Mater Sci 32:67–109

105. Luo J, Chiang YM, Cannon RM (2005) Nanometer-thick surficial films in oxides as a case of prewetting. Langmuir 21:7358–7365

106. Wong J (1974) Nature of intergranular phase in nonohmic ZnO ceramics containing 9.5 mol percent Bi_2O_3. J Am Ceram Soc 57:357–359

107. Wong J, Morris WG (1974) Microstruture and phases in nonohmic ZnO–Bi_2O_3 ceramics. Am Ceram Soc Bull 53:816–820

108. Greuter F (1995) Electrically active interfaces in ZnO varistors. Sol State Ionics 75:67–78

109. Gambino JP, Kingery WD, Pike GE, Philipp HR (1989) Effect of heat-treatments on the wetting behaviour of bismuth-rich intergarnular phases in ZnO–Bi–Co varistors. J Am Ceram Soc 72:642–645

110. Kingery WD, van der Sande JB, Mitamura T (1979) STEM investigation of grain boundary segregation in a ZnO–Bi_2O_3 varistor. J Am Ceram Soc 62:221–222

111. Olsson E, Falk LKL, Dunlop GL (1985) The microstructure of a ZnO varistor material. J Mater Sci 20:4091–4098. doi:10.1007/BF00552403

112. Olsson E, Dunlop GL (1989) Characterization of individual interfacial barriers in a ZnO varistor material. J Appl Phys 66:3666–3675

113. Matsuoka M (1971) Nonohmic properties of zinc oxide ceramics. Jpn J Appl Phys 10:736–742

114. Luo J, Chiang YM (2008) Wetting and prewetting on ceramic surfaces. Annu Rev Mater Res 38:227–249

115. Luo J, Chiang YM (2000) Existence and stability of nanometer-thick disordered films on oxide surfaces. Acta Mater 48:4501–4515

116. Qian H, Luo J (2007) Vanadia-based equilibrium-thickness amorphous films on anatase (101) surfaces. J Appl Phys Lett 91:061909

117. Qian H, Luo J, Chiang YM (2008) Anisotropic wetting of ZnO by Bi_2O_3 with and without nanometer-thick surficial amorphous films. Acta Mater 56:862–873